Aluminum-Doped Perovskites As High-Performance Oxygen Permeation Materials

Julia Martynczuk,*[,†] Fangyi Liang,[†] Mirko Arnold,[†] Vladimir Šepelák,[‡,§] and Armin Feldhoff[†]

Institute of Physical Chemistry and Electrochemistry, Leibniz Universität Hannover, D-30167 Hannover, Germany, and Institute of Physical and Theoretical Chemistry, Braunschweig University of Technology, D-38106 Braunschweig, Germany

Received November 28, 2008. Revised Manuscript Received February 12, 2009

Previously unreleased compositions of $(Ba_{0.5}Sr_{0.5})(Fe_{1-x}Al_x)O_{3-\delta}$ perovskites in the range of $0 \leq x \leq 0.2$ were synthesized and studied with respect to electronic and crystallographic structure, as well as oxygen permeation. The perovskite phase in all synthesized oxides was found to be cubic, without any impurities for aluminum fractions in the range $x = 0.01-0.09$. Electron energy-loss spectroscopy (EELS) revealed a significant amount of covalency by Fe-3d−O-2p hybridization and a mixed Fe^{3+} /Fe^{4+} valence state of iron for all synthesized perovskites, which was quantified by Mössbauer spectroscopy. Trivalent aluminum replaces a higher fraction of Fe^{4+} than of Fe^{3+} while both iron species are in high-spin state. The Mössbauer quadrupole splittings indicate a greater disorder around iron with increasing aluminum content and, together with the EELS result of an abatement of covalent character in the bonding of iron and oxygen, the observed lattice expansion can be understood. In situ XRD and TG/DTA measurements revealed high temperature stability of the materials up to 1350 °C. The oxygen permeation increases with rising aluminum content from 0 to 0.1, and the $(Ba_{0.5}\ Sr_{0.5})(Fe_{0.9}Al_{0.1})O_{3-\delta}$ membranes show a very high oxygen permeation (1.19 mL cm^{-2} min^{-1} at 950 °C) compared to known perovskite membranes. Even among the previously published iron and aluminum containing membranes, they exhibit the highest oxygen permeation.

Introduction

Many industrial processes require the supply or removal of oxygen to or from reaction mixtures with high selectivity and oxygen fluxes. The separation of oxygen from air by ceramic membranes is a key technology. Membranes with both high flux and selectivity are based on mixed ionic-electronic conductors (MIECs) with perovskite structure.[1,2] Perovskite-type oxides of the composition ABO_3 can host many different cations on the A- and B-sites, which enables us to tune conductivities from almost pure electronic to almost pure ionic. Numerous applications of perovskite membranes with different elemental compositions have already been reported, e.g., separation of oxygen from air, partial oxidation of hydrocarbons and oxygen-enrichment in air.[3−8] The electrochemical importance of perovskite oxides is apparent in the case of solid-oxide fuel cells (SOFCs) for power generation.[9] In this application, perovskites are employed as cathode, electrolyte or anode materials, and even full ceramic intermediate-temperature solid oxide fuel cells (IT-SOFCs, ca. 500−800 °C) are possible.[10−14] For membrane-based dehydrogenation processes in the synthesis of basic chemicals like ethylene[15] and propylene[16] at high selectivity, and for IT-SOFCs,[17] the long-time stability of the materials is of special interest. However, perovskite materials offer, in addition to oxygen separation membranes, an even wider range of application in many different fields, which are listed elsewhere.[18]

Because of their multiple applications, new perovskite materials are of major interest for natural scientists, like chemists and materials scientists. The current state-of-the-

* Corresponding author. E-mail: julia.martynczuk@pci.uni-hannover.de.
† Leibniz Universität Hannover.
‡ Braunschweig University of Technology.
§ On leave from the Slovak Academy of Sciences, Košice, Slovakia.

(1) Merkle, R.; Maier, J.; Bouwmeester, H. J. M. *Angew. Chem., Int. Ed.* **2004**, *43*, 5069–5073.
(2) Sunarso, J.; Baumann, S.; Serra, J. M.; Meulenberg, W. A.; Liu, S.; Lin, Y. S.; Diniz da Costa, J. C. *J. Membr. Sci.* **2008**, *320*, 13–41.
(3) Liu, M.; Joshi, V.; Shen, Y.; Krist, K. U.S. Patent 5 273 628, 1993.
(4) Balachandran, U.; Dusek, J. T.; Mieville, R. L.; Poeppel, R. B.; Kleefisch, M. S.; Pei, S.; Kobylinski, T. P.; Udovich, C. A.; Bose, A. C. *Appl. Catal., A* **1995**, *133*, 19–29.
(5) Wang, H.; Cong, Y.; Yang, W. *J. Membr. Sci.* **2002**, *209*, 143–152.
(6) Wang, H.; Cong, Y.; Zhu, X.; Yang, W. *React. Kinet. Catal. Lett.* **2003**, *79*, 351–356.
(7) Hamel, C.; Seidel-Morgenstern, A.; Schiestel, T.; Werth, S.; Wang, H.; Tablet, C.; Caro, J. *AIChE J.* **2006**, *52*, 3118–3125.
(8) Wang, H.; Werth, S.; Schiestel, T.; Caro, J. *Angew. Chem., Int. Ed.* **2005**, *44*, 6906–6909.
(9) Yokokawa, H.; Sakai, N.; Kawada, T.; Dokiya, M. *Solid State Ionics* **1992**, *52*, 43–56.
(10) Shao, Z.; Haile, S. *Nature* **2004**, *431*, 170–173.
(11) Esquirol, A.; Brandon, N. P.; Kilner, J. A.; Mogensen, M. *J. Electrochem. Soc.* **2004**, *151*, A1847−A1855.
(12) Tao, S.; Irvine, J. T. S. *Adv. Mater.* **2006**, *18*, 1581–1584.
(13) Fu, Q. X.; Tietz, F.; Stöver, F. *J. Electrochem. Soc.* **2006**, *153*, D74−D83.
(14) Hsu, M.-F.; Wu, L.-J.; Wu, J.-M.; Shiu, Y.-H.; Lin, K.-F. *Electrochem. Solid-State Lett.* **2006**, *9*, A193−A195.
(15) Wang, H.; Cong, Y.; Yang, W. *Chem. Commun.* **2002**, 1468–1469.
(16) Vente, J.; McIntosh, S.; Haije, W.; Bouwmeester, H. J. W. *React. Kinet. Catal. Lett.* **2003**, *79*, 351–356.
(17) Steele, C.; Heinzel, A. *Nature* **2001**, *414*, 345–352.
(18) Martynczuk, J.; Arnold, M.; Wang, H.; Caro, J.; Feldhoff, A. *Adv. Mater.* **2007**, *19*, 2134–2140.

10.1021/cm803217t CCC: $40.75
Published on Web 03/26/2009

art material, because of its high oxygen permeation flux and phase stability above 900 °C, is $(Ba_{0.5}Sr_{0.5})(Co_{0.8}Fe_{0.2})O_{3-\delta}$ (BSCF).[1,10,19] However, recently, serious stability problems with cobalt-containing materials in the IT range have been discussed in the literature.[20,21] If the cubic BSCF is kept at temperatures below 900 °C for long time periods, a decomposition into a three-phase mixture takes place because of a reversible reordering of the hexagonal AO_3-layer stacking sequence in the cubic perovskite. The breakdown of the cubic perovskite structure leads to the long-term instability of the BSCF material in the IT range. The driving force for this reaction was identified to be the cobalt site (Co^{2+}/Co^{3+}), because trivalent cobalt shows a high-spin (HS) to low-spin (LS) transition and prefers a low-spin configuration at intermediate temperatures. Furthermore, it was shown by in situ high-temperature electron energy-loss spectroscopy (HT-EELS) on BSCF[22] and comparative TGA of different perovskite-type materials[23] that the redox behavior of polyvalent B-site cobalt ions is much more flexible than that of iron, manganese, or nickel. The flexible redox behavior of cobalt in BSCF causes a large coefficient of thermal expansion (CTE) in the range of $20-24 \times 10^{-6}$ K^{-1},[24,25] resulting in huge thermal stresses and, in the worst case, crack formation.

Therefore, the search for alternative materials and the development of cobalt-free perovskite-type oxides are of great interest. The introduction of lower valence state ions into the perovskite structure ABO_3 induces oxygen vacancies, leading to an improved ionic conductivity that benefits the oxygen permeability. This paper presents novel cobalt-free perovskite materials of $A^{II}B^{III/IV}$ $O_{3-\delta}$-type, containing iron and aluminum with the stoichiometries $(Ba_{0.5}Sr_{0.5})(Fe_{1-x}Al_x)O_{3-\delta}$ (BSFA). Doping of the B-site of the perovskite structure with a metal with a fixed valence state, like the trivalent aluminum, is expected to lead to the diminution of nonstoichiometric oxygen variations and a more stable redox behavior of the material. The lattice expansion caused by the variation in temperature or chemical oxygen potential is likely to be reduced, but the oxygen permeability due to higher ionic conductivity should improve.

We are not the first to investigate the idea of aluminum doping. There are several lanthanum-based[26−33] as well as strontium-based[32−46] aluminum-doped perovskite materials reported in the literature. Even though Holc et al. suggest $(La_{0.8}Sr_{0.2})(Fe_{1-x}Al_x)O_{3-\delta}$ with $x = 0$, 0.3, and 0.5 as candidates for IT-SOFCs,[26] most researchers have reported a deterioration in the oxygen permeation for lanthanum-based aluminum doped perovskite materials, e.g., for $(La_{0.5}Sr_{0.5})FeO_{3-\delta}$, $(La_{1-x}Ca_x)(Al_yFe_{1-y})O_{3-\delta}$, and $La(Ga_{0.9-x}Mg_{0.1}Al_x)O_{3-\delta}$.[29,30,32] A decrease in the ionic and electronic conductivity was also published for strontium-based aluminum-doped perovskites by Dong et al. for $Sr(Co_{0.4}Fe_{0.6-x}Al_x)O_{3-\delta}$ and Kharton et al. for $(Sr_{0.7}La_{0.3})(Fe_{1-x}Al_x)O_{3-\delta}$, $Sr(Fe_{1-y}Al_y)O_{3-\delta}$, and $(Sr_{0.7}La_{0.3})(Co_{0.8}Al_{0.2})O_{3-\delta}$.[35−38] To the best of our knowledge, the only barium-containing aluminum-doped perovskite reported in the literature is $(Sr_{0.8}Ba_{0.2})(Co_{0.5}Al_{0.3}Fe_{0.2})O_{3-\delta}$, and only the coefficient of thermal expansion (CTE: 22.4×10^{-6} K^{-1} for $773 \leq T \leq 1273$ K) for this cobalt-containing material is tabulated.[46]

The structural characterization of the novel $(Ba_{0.5}Sr_{0.5})(Fe_{1-x}Al_x)O_{3-\delta}$ material was carried out by (in situ) X-ray diffraction (XRD) and Rietveld refinements. Electron energy-loss spectroscopy (EELS) and Mössbauer spectroscopy revealed the iron oxidation and spin-states and the hybridization of iron and oxygen. Scanning electron microscopy (SEM), combined with energy-dispersive X-ray spectroscopy (EDXS) and transmission electron microscopy (TEM) along with EDXS, were conducted to examine the microstructure

(19) Shao, Z.; Yang, W.; Cong, Y.; Dong, H.; Tong, J.; Xiong, G. *J. Membr. Sci.* **2000**, *172*, 177–188.
(20) Arnold, M.; Gesing, T. M.; Martynczuk, J.; Feldhoff, A. *Chem. Mater.* **2008**, *20*, 5851–5858.
(21) Švarcová, S.; Wiik, K.; Tolchard, J.; Bouwmeester, H. J. M.; Grande, T. *Solid State Ionics* **2008**, *178*, 1787–1791.
(22) Arnold, M.; Xu, Q.; Tichelaar, F. D.; Feldhoff, A. *Chem. Mater.* **2009**, *21*, 635−640.
(23) Teraoka, Y.; Shimokawa, H.; Kang, C.; Kusaba, H.; Sasaki, K. *Solid State Ionics* **2006**, *177*, 2245–2248.
(24) McIntosh, S.; Vente, J.; Haije, W.; Blank, D.; Bouwmeester, H. J. W. *Chem. Mater.* **2006**, *18*, 2187–2193.
(25) Vente, J.; Haije, W.; Rak, Z. *J. Membr. Sci.* **2006**, *276*, 178–184.
(26) Holc, J.; Kuščer, D.; Hrovat, M.; Bernik, S.; Kolar, D. *Solid State Ionics* **1997**, *95*, 259–268.
(27) Ciambelli, P.; Cimino, S.; Lasorella, G.; Lisi, L.; De Rossi, S.; Faticanti, M.; Minelli, G.; Porta, P. *Appl. Catal., B* **2002**, *37*, 231–241.
(28) Park, H. J.; Choi, G. M. *Solid State Ionics* **2004**, *175*, 399–403.
(29) Cihlar, J.; DelFavero, D.; Cihlar, J., Jr.; Buchal, A.; van Herle, J. *J. Eur. Ceram. Soc.* **2006**, *26*, 2999–3004.
(30) Kajitani, M.; Matsuda, M.; Miyake, M. *Solid State Ionics* **2007**, *178*, 355–358.
(31) Urasaki, K.; Fukuda, Y.; Sekine, Y.; Matsukata, M.; Kikuchi, E. *J. Jpn. Pet. Inst.* **2008**, *51* (2), 83–87.
(32) Kharton, V. V.; Shaula, A. L.; Snijkers, F. M. M.; Cooymans, J. F. C.; Luyten, J. J.; Marozau, I. P.; Viskup, A. P.; Marques, F. M. B.; Frade, J. R. *J. Eur. Ceram. Soc.* **2006**, *26*, 3695–3704.
(33) Kharton, V. V.; Waerenborgh, J. C.; Viskup, A. P.; Yakovlev, S. O.; Patrakeev, M. V.; Gaczyńskic, P.; Marozau, I. P.; Yaremchenko, A. A.; Shaula, A. L.; Samakhval, V. V. *J. Solid State Chem.* **2006**, *179*, 1273–1284.
(34) Dunyushkina, L. A.; Gorbunov, V. A.; Babkina, A. A.; Esina, N. O. *Ionics* **2003**, *9*, 67–70.
(35) Yaremchenko, A. A.; Patrakeev, M. V.; Kharton, V. V.; Marques, F. M. B.; Leonidov, I. A.; Kozhevnikov, V. L. *Solid State Sci.* **2004**, *6*, 357–366.
(36) Shaula, A. L.; Kharton, V. V.; Vyshatko, N. P.; Tsipis, E. V.; Patrakeev, M. V.; Marques, F. M. B.; Frade, J. R. *J. Eur. Ceram. Soc.* **2005**, *25*, 489–499.
(37) Kharton, V. V.; Tsipis, E. V.; Yaremchenko, A. A.; Marozau, I. P.; Viskup, A. P.; Frade, J. R.; Naumovich, E. N. *Mater. Sci. Eng., B* **2006**, *134*, 80–88.
(38) Dong, X.; Xu, Z.; Chang, X.; Zhang, C.; Jin, W. *J. Am. Ceram. Soc.* **2007**, *90* (12), 3923–3929.
(39) Takamura, H.; Enomoto, K.; Aizumi, Y.; Kamegawa, A.; Okada, M. *Solid State Ionics* **2004**, *175*, 379–382.
(40) Waerenborgh, J. C.; Rojas, D. P.; Shaula, A. L.; Mather, G. C.; Patrakeev, M. V.; Kharton, V. V.; Frade, J. R. *Mater. Lett.* **2005**, *59*, 1644–1648.
(41) Kharton, V. V.; Shaula, A. L.; Snijkers, F. M. M.; Cooymans, J. F. C.; Luyten, J. J.; Yaremchenko, A. A.; Valente, A. A.; Tsipis, E. V.; Frade, J. R.; Marques, F. M. B.; Rocha, J. *J. Membr. Sci.* **2005**, *252*, 215–225.
(42) Yaremchenko, A. A.; Kharton, V. V.; Shaula, A. L.; Snijkers, F. M. M.; Cooymans, J. F. C.; Luyten, J. J.; Marques, F. M. B. *J. Electrochem. Soc.* **2006**, *153* (6), J50–J60.
(43) Patrakeev, M. V.; Kharton, V. V.; Bakhteeva, Y. A.; Shaula, A. L.; Leonidov, I. A.; Kozhevnikov, V. L.; Naumovich, E. N.; Yaremchenko, A. A.; Marques, F. M. B. *Solid State Sci.* **2006**, *8*, 476–487.
(44) Naumovich, E. N.; Patrakeev, M. V.; Kharton, V. V.; Islam, M. S.; Yaremchenko, A. A.; Frade, J. R.; Marques, F. M. B. *Solid State Ionics* **2006**, *177*, 457–470.
(45) Marozau, I. P.; Kharton, V. V.; Viskup, A. P.; Frade, J. R.; Samakhval, V. V. *J. Eur. Ceram. Soc.* **2006**, *26*, 1371–1378.
(46) Ancharova, U. V.; Ancharov, A. I.; Lyakhov, N. Z.; Nemudry, A. P.; Pyatiletova, E. B.; Savinskaya, O. A.; Tsybulya, S. V. *Nucl. Instrum. Methods Phys. Res., Sect. A* **2007**, *575*, 144–148.

and elemental composition. Additionally, differential thermal analysis (DTA) and oxygen permeation experiments were conducted for characterization purposes.

Experimental Section

$(Ba_{0.5}Sr_{0.5})(Fe_{1-x}Al_x)O_{3-\delta}$ powders were synthesized by a combined citric acid and ethylene-diamine-tetraacetic acid (EDTA) method, as described in detail elsewhere.[18,47,48] Given amounts of $Ba(NO_3)_2$, $Zn(NO_3)_2$, $Fe(NO_3)_3$, and $Sr(NO_3)_2$ were dissolved in water, followed by the addition of EDTA acid and citric acid with the EDTA acid:citric acid:total of metal cations molar ratio controlled at around 1:1.5:1. After agitation for a given time, the pH value of the solution was adjusted to approximately 9, by the addition of $NH_3 \cdot H_2O$. Water was evaporated with stirring at 150 °C. The transparent solution transformed into a dark purple gel following several hours of evaporation. Further heat treatments were applied, i.e., the precalcination for 2 h at ca. 700 °C and the final calcination to obtain the pure perovskite phases for 10 h at 950 °C. The calcined powders were uniaxially pressed under 140 kN into pellets and sintered pressurelessly at 1150 °C for 10 h to ceramic discs of 14 mm in diameter and a thickness of 1.1 mm.

X-ray diffraction (XRD) was measured with a Philips X'pert-MPD instrument using a flat sample geometry and monochromator-filtered Cu Kα radiation at 40 kV and 40 mA, a receiving slit of 0.19−0.38 mm and count times of 3−25 s per step. Data were collected in a step-scan mode in the range of 15−100° with intervals of 0.005 to 0.03°. Data for interpretation were taken from the PDF-2 database with PDF numbers $BaAl_2O_4$ [17−306] and $Ba_3Al_2O_6$ [25−75]. In situ XRD measurements were taken with steps of 200 K with a heating rate of 5 K/min, respectively, in order to achieve a good overview within the temperature range 35−1000 °C. Before each data acquisition, an equilibrium time of 1/2 h was set, five scans were performed at 1000 °C, and the temperature was held for 10 h. Ambient air was used as the atmosphere within the chamber. Rietveld refinements on the XRD powder data were carried out by using Topas Academic 4.1 software. During refinements, general parameters, such as the scale factor, background parameters, and the zero point of the counter, were optimized. Profile shape calculations were carried out using the Thompson−Cox−Hastings function implemented in the program by varying the strain parameter as well. Additionally, the cell parameter and the displacement parameters were refined. In the case of site occupation with mixed atoms, linear constraints were used for the occupancy (the occupancy of atom B is equivalent to 1.0 minus the occupancy of atom A) and the displacement parameters (atoms on the same position have the same displacement parameter).

^{57}Fe Mössbauer spectroscopic measurements were performed in transmission geometry using a conventional spectrometer in constant acceleration mode at temperature $T = 293$ K. A ^{57}Co/Rh γ-ray source was used. The velocity scale of the spectra was calibrated relative to ^{57}Fe in Rh. "Recoil" spectral analysis software[49] and the Voigt-based fitting method were used for the quantitative evaluation of the Mössbauer spectra. A Lorentzian line width of 0.30 mm/s, resulting from the fit of the spectrum of the BSF sample, was chosen for fitting the spectra of the other investigated samples.

Scanning electron microscopy (SEM) was performed with a JEOL JSM-6700F. Secondary electron (SE) micrographs were taken at a low excitation voltage of 2 kV. To analyze the microstructure of the sintered membranes, we conducted SEM on both surfaces and on fracture surfaces, and grain size distributions were evaluated using image analysis software (Adobe Photoshop CS2 (version 9.0) and ImageJ (1.33 u)).[50] Fracture surfaces were etched with aqueous HCl (0.5 M) for 1−2 min in order to visualize grain boundaries. An EDX spectrometer, Oxford Instruments INCA-300, with an ultrathin window was used for elemental analysis.

Thermogravimetric analysis (TGA) and differential thermal analysis (DTA) were measured on calcined BSFA powders in DTA/TG crucibles of Al_2O_3 with a SETSYS TGA-DSC instrument from 20 to 1200 °C with a heating rate of 20 K/min and from 1200 to 1420 °C with a heating rate of 1 K/min under air (flowrate: 100 mL/min).

Transmission electron microscopy (TEM) and electron energy-loss spectroscopy (EELS) were conducted at 200 kV with a JEOL JEM-2100F-UHR field-emission instrument equipped with a Gatan GIF 2001 energy filter and a 1k-CCD camera. EDXS was carried out by a light-element detector using the Cliff-Lorimer quantification technique (INCA 200 TEM, Oxford Instruments). EELS was performed in diffraction coupled mode while taking care to measure accurately the absolute position of core-loss details.[51] The preparation of standards for Fe^{4+} ($SrFeO_3$) and Fe^{3+} (α-Fe_2O_3), which were carefully checked by Mössbauer spectroscopy to exhibit only the desired iron valence, is described elsewhere.[51] Furthermore, the specimen for TEM investigations was prepared similar to Martynczuk et al.[50] Membranes were cut, covered on both sides with silicon single crystals, polished on polymer embedded diamond lapping films, and epoxy-glued onto a copper slot grid. Electron transparency was achieved by Ar^+ ion sputtering (Gatan, model 691 PIPS).

The oxygen permeation was measured in a high-temperature permeation cell[52] from 800 to 950 °C in steps of 25 °C with an equilibrium time of 15 min. Discs were sealed onto a ceramic tube with gold-paste (conducting 130 paste, C5754, Heraeus) at 950 °C for 2 h. The actual temperature was measured 1 cm above the membrane with a quartz glass protected Pt/Rh thermocouple. After sealing, gas flow rates were delivered to the reactor by mass flow controllers (Bronckhorst Hi-Tech) and continuously read by an online gas chromatograph (Agilent Technologies, HP 5890, equipped with a Carboxen 1000 column). The detection of the gases in the chromatograph took 7 min each and at each temperature up to six detections were done; thus, the maximum time at one temperature was 49 min. Air was fed at a rate of 150 mL min^{-1} to the air side; He (29.0 mL min^{-1}, 99.995%) and Ne (1.0 mL min^{-1}, 99.995%) as the internal standard gases were fed to the sweep side. The absolute flow rate of the effluents was determined by using neon as an internal standardization. For that purpose, the concentration of neon in the effluents was measured. Because the flow rate of neon is known, it is thus possible to calculate the total flow rate of the effluents. Nitrogen was also detected in the effluents by gas chromatography because of slight imperfections in the sealing, and the leakage of oxygen was subtracted in the calculation of the oxygen permeation flux. The relative leakage of O_2 was found to be less than 5%. The permeation flux through the membrane could

(47) Feldhoff, A.; Martynczuk, J.; Wang, H. *Prog. Solid State Chem.* **2007**, *35*, 339–353.
(48) Arnold, M.; Wang, H.; Martynczuk, J.; Feldhoff, A. *J. Am. Ceram. Soc.* **2007**, *90* (11), 3651–3655.
(49) Lagarec, K.; Rancourt, D. G. *Recoil−Mössbauer Spectral Analysis Software for Windows, version 1.02*; Department of Physics, University of Ottawa: Ottawa, ON, 1998.
(50) Martynczuk, J.; Arnold, M.; Feldhoff, A. *J. Membr. Sci.* **2008**, *322*, 375–382.
(51) Feldhoff, A.; Martynczuk, J.; Arnold, M.; Myndyk, M.; Bergmann, I.; Šepelák, V.; Gruner, W.; Vogt, U.; Hähnel, A.; Woltersdorf, J. *Chem. Mater.* **2009**, submitted.
(52) Wang, H.; Tablet, C.; Feldhoff, A.; Caro, J. *J. Membr. Sci.* **2005**, *262*, 20–26.

Table 1. Tolerance Factors of BSFA with the Assumption of Sole Fe^{3+}, Sole Fe^{4+}, or with the Ratio of Fe^{3+} /Fe^{4+} Both in High-Spin State Calculated from Integral Intensities of ^{57}Fe Mössbauer Subspectra[a]

	tolerance factor *t*			elemental fractions		
	Fe^{3+}	Fe^{3+} /Fe^{4+}	Fe^{4+}	Fe^{3+}	Fe^{4+}	Al^{3+}
BSF	1.011	1.022	1.042	63.6	36.4	0
BSFA0.01	1.012	1.023	1.042	63.9	35.1	1
BSFA0.05	1.014	1.024	1.043	62.7	32.3	5
BSFA0.1	1.019	1.025	1.046	61.7	28.9	9.4
BSFA0.2	1.022	1.033	1.047	44.4	35.6	20

[a] For the aluminum fractions, mean values were calculated by EDX measurements for each composition at 10 different positions of the specimen.

then be calculated by the fraction of O_2 in the effluents and the determination of the effective permeation area of the membrane.

Results and Discussion

The incorporation of aluminum into the perovskite lattice was conducted systematically. Because of the small ionic radius of trivalent aluminum ($r(Al^{3+}) = 0.535$ Å), it was expected to be incorporated at the B-position of ABO_3 (A: $r(Ba^{2+}) = 1.61$ Å, $r(Sr^{2+}) = 1.44$ Å, B: $r(Fe^{3+}, HS) = 0.645$ Å, $r(Fe^{4+}, HS) = 0.585$ Å, $r(O^{2-}) = 1.40$ Å).[53] A good benchmark for the degree of aluminum doping in a cubic perovskite is the tolerance factor *t* described by Goldschmidt.[54] For the ideal cubic structure, *t* should equal one. It was adapted to double perovskites by Anderson[55] and can be calculated for ABO_3 with weighted arithmetic mean values for the cationic radii $\bar{r}$ according to Feldhoff et al.[47]

$$t = \frac{\bar{r}_A + r_O}{\sqrt{2}[\bar{r}_B + r_O]} \quad (1)$$

For the composition $(Ba_{0.5}Sr_{0.5})(Fe_{1-x}Al_x)O_{3-\delta}$, the values for *t* are labeled in Table 1 for Fe^{3+}, Fe^{4+}, and for the ratio of Fe^{3+} to Fe^{4+} determined by Mössbauer spectroscopy. The values for *t* are in the range of 1.01−1.05 for $0 \leq x \leq 0.2$. When the tolerance factor is $t > 1$, the AO_3 layers typically adopt mixed cubic and hexagonal, or pure hexagonal, close-packed stacking sequences.[20,56] The more *t* deviates from unity, the less stable the cubic perovskite; thus, it is reasonable to expect a cubic perovskite with very low aluminum doping. Apparently, the maximum aluminum doping for BSFA is around $x = 0.1$ with a tolerance factor of 1.025. This conclusion can be drawn from Figure 1. The crystal structure of the synthesized powders with various aluminum fractions calcined at 950 °C for 10 h was examined by X-ray powder diffraction from 20 to 60° 2θ at room temperature (Figure 1a). The oxides with aluminum fractions of $0 \leq x \leq 0.05$ crystallize as cubic perovskites with lattice parameters around 0.396 nm, which are labeled in 1b in a zoom of reflex at the Miller index (110) for lattice parameter determination. The perovskite phase in all synthesized oxides is cubic perovskite, and the highest aluminum fraction for a formation of pure cubic perovskite without any impurities is in the range of $x = 0.09-0.1$. The BSFA oxides with aluminum fractions of $x \geq 0.1$ do not form a pure cubic perovskite phase. In the BSFA0.1 powder a minor impurity (3.3%) of $BaAl_2O_4$ was determined by Rietveld refinements (Figure 2).

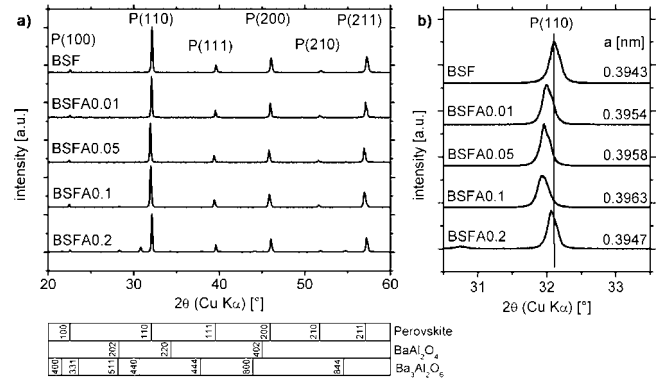

Figure 1. X-ray diffraction data of (a) all synthesized BSFA oxides with various aluminum fractions calcined at 950 °C for 10 h, (b) zoom of reflex at the Miller index (110) for determination of lattice parameters a. Reflex positions for perovskite (p) belong to BSF with $a = 0.3943$ nm.

The Rietveld refinement of BSFA0.1 revealed a two-phase mixture consisting of the perovskite and a second oxide ($BaAl_2O_4$). The perovskite was found to crystallize in the cubic space group $Pm\bar{3}m$ (No. 221) with a lattice parameter of 0.39630(3) nm. Barium and strontium were refined on the same crystallographic position 1a (0,0,0) with 52(2)% occupation for the strontium atoms corresponding to the chemical analysis and a displacement parameter of $B = 1.3$ (1). Iron (91%) and aluminum (9%) were calculated at the 1b (1/2,1/2,1/2) position, showing a high displacement of $B = 1.7(1)$. An equivalently high displacement of $B = 2.8$ (5) was found for the oxygen atoms on the 3c (0,1/2,1/2) site. The refinement converged to reliability factors of RWP = 0.127 and RP = 0.09 for the pattern with a goodness of fit = 1.265, a Durban−Watson parameter of 1.345, and a Bragg *R*-value of 0.022 for the perovskite structure.

The second oxide was identified as hexagonal $BaAl_2O_4$ with space group $P6_322$ (No. 182), as reported by Arlett et al.[57] Quantitative analysis revealed that the perovskite structure is the major phase, accounting for 96.7%, and the $BaAl_2O_4$ accounts for 3.3%. For BSFA0.2 two impurities were found and identified as 6% of hexagonal $BaAl_2O_4$ and 8% of cubic $Ba_3Al_2O_6$[58] with space group Pa_3 (No. 205, Figure 1a). The tolerance factor is nevertheless a good benchmark for the predictability of perovskite formation. When the aluminum fraction was higher than 0.1 ($t \geq 1.025$),

(53) Shannon, R. D. *Acta Crystallogr., Sect. A* **1976**, *32*, 751–767.
(54) Goldschmidt, V. M. *Naturwissenschaften* **1926**, *14*, 477–485.
(55) Anderson, M. T.; Greenwood, K. B.; Taylor, G. A.; Poeppelmeier, K. R. *Prog. Solid State Chem.* **1993**, *22*, 197–233.
(56) Davies, P. K.; Wu, H.; Borisevich, A. Y.; Molodetsky, I. E.; Farber, L. *Annu. Rev. Mater. Res.* **2008**, *38*, 369–401.
(57) Arlett, R. H.; White, J. G.; Robbins, M. *Acta Crystallogr.* **1967**, *22*, 315.
(58) Hilpert, K.; Beske, H.; Naoumidis, A. *High Temp. Sci.* **1975**, *7* (3), 159–166.

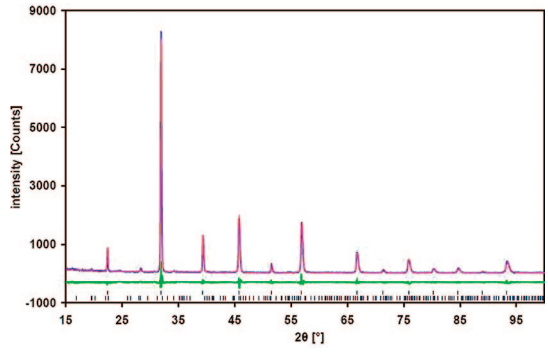

Figure 2. Rietveld refinement for BSFA0.1 (calcined at 950 °C for 10 h). The observed (blue) and calculated intensities (red) together with the difference (green) between the observed and calculated pattern as well as the possible reflex position (tick marks) are given.

the aluminum was not completely incorporated into the perovskite lattice, and instead of a hexagonal perovskite, the excessive aluminum formed an extra hexagonal phase containing predominantly barium at the A-site. For this reason, the BSFA0.2 perovskite does not contain an Al fraction of $x = 0.2$, but rather less than that, and therefore, the lattice constant decreases again. Astonishingly, the lattice parameter increases with higher aluminum doping ($x \leq 0.1$, Figure 1b), although a decrease due to the smaller ionic radius of aluminum could be expected. Hence, this aspect cannot be explained by the assumption of a purely ionic crystal, but by the results of EELS.

To investigate the electronic structure, we examined the iron $L_{2,3}$- (Figure 3a) and oxygen K-edge (Figure 3b) by EELS measurements. The iron $L_{2,3}$-edge displays an electronic transition from the Fe-2p core orbitals to the partly unoccupied Fe-3d orbitals (energetic location displayed schematically in Feldhoff et al.[51]). The validity of the dipole selective rule in principle attributes the sensitivity of this measurement to the chemical environment of iron with respect to coordination, valence, and spin configuration.[59] Figure 3a shows no significant changes of the overall shape and position of the iron $L_{2,3}$-edge for the different BSFA samples. However, compared to standards for Fe^{4+} ($SrFeO_3$) and Fe^{3+} (α-Fe_2O_3), all BSFA samples show a smaller fwhm of the L_3 white line. That indicates a mixed valence of Fe^{3+}/Fe^{4+} and a small energy difference between the intra-atomic exchange splitting and the cubic crystal field splitting, making a competition of iron high-spin and low-spin states likely. The presence of Fe^{2+} or Fe^{6+} can be excluded. The oxygen K-edge is caused by the transition of oxygen 1s orbitals into orbitals with oxygen 2p character. If the iron 3d orbitals are hybridized with the oxygen 2p ligand orbitals, the energy-loss near-edge structure of the oxygen K-edge also reflects the occupation of the iron 3d orbitals. That means the charge distribution between oxygen and iron is reflected in both the iron $L_{2,3}$-edge and the oxygen K-edge.[60] Figure 3b displays the oxygen K-edge, which is separated into three parts: the low energy part A (525−532 eV), reflecting the hybridization of the oxygen 2p orbitals with the partly occupied iron 3d

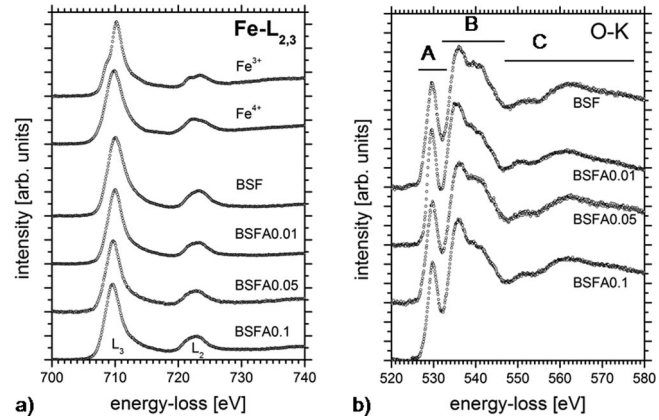

Figure 3. Room-temperature EEL spectra (a) of the Fe-$L_{2,3}$ edge for BSF, BSFA0.01, BSFA0.05, and BSFA0.1 compared to Fe^{3+} and Fe^{4+} standards, (b) of the O−K edge for BSF, BSFA0.01, BSFA0.05, and BSFA0.1.

orbitals; a middle energy part B (532−547 eV), reflecting the hybridization of the oxygen 2p orbitals with the barium 4f, strontium 4d, and aluminum 3p orbitals; and the high energy part C (above 547 eV), reflecting the hybridization with the empty iron 4sp band.[51,61,62] The occurrence of the A peak of the O K-edge leads to the conclusion that there is a significant amount of covalency due to the iron 3d−oxygen 2p hybridization. As the formal valence of iron decreases, the occupation of the hybridized 3d orbitals with the oxygen 2p ligand is diminished. Therefore, the probability of exciting a core electron into these orbitals is lower. This is reflected in the peak area.[63,64] The intensity ratio B/A follows from estimating the integral intensities in the energy-loss intervals 532−547 and 525−532 eV. It increases from 4.55 (BSF) to 5.26 (BSFA0.1). Thus, the hybridization of Fe-3d with O-2p decreases slightly relatively to that of the other cations (Ba-4f, Sr-4d, Al-3p). Obviously, aluminum takes part in the charge transfer, and thus, the covalent mixing of iron and oxygen orbitals decreases, leading to the extension of the lattice with increasing aluminum content.

The mixed Fe^{3+}/Fe^{4+} valence state of iron can be quantified by Mössbauer spectroscopy. Panels a and b in Figure 4 show the Mössbauer room-temperature spectra of BSFA with $0 \leq x \leq 0.2$ and the variation in the amount of Fe^{3+} and Fe^{4+} cations in the BSFA samples as a function of aluminum content. The spectra of the BSF, BSFA0.01, BSFA0.05, and BSFA0.1 samples were fitted with two doublets, with the values of isomer shift of −0.17 and 0.18 mm/s characteristic of tetravalent (Fe^{4+}) and trivalent (Fe^{3+}) cations, both in the high-spin state, respectively.[51,65,66] Note that the isomer shift values corresponding to Fe^{4+} cations are in agreement with those reported for $SrFe_{1-x}Al_xO_{3-\delta}$.[40] The spectrum of the BSFA0.2 sample, however, is not well fitted with only two

(59) Egerton, R. F. *Electron Energy-Loss Spectroscopy in the Transmission Electron Microscope*; Plenum Press: New York, 1986.
(60) de Groot, F.M.F.; Grioni, M.; Fuggle, J. C.; Ghijsen, J.; Sawatzky, G. A.; Petersen, H. *Phys. Rev. B* **1989**, *40*, 5715–5723.
(61) Samantaray, C. B.; Sim, H.; Hwang, H. *Appl. Surf. Sci.* **2005**, *242*, 121–128.
(62) Sasakia, T.; Mizoguchi, T.; Matsunaga, K.; Tanaka, S.; Yamamoto, T.; Kohyama, M.; Ikuhara, Y. *Appl. Surf. Sci.* **2005**, *241*, 87–90.
(63) Gloter, A.; Ingrin, J.; Bouchet, D.; Colliex, C. *Phys. Rev. B* **2000**, *61*, 2587–2594.
(64) Colliex, C.; Manoubi, T.; Ortiz, C. *Phys. Rev. B* **1991**, *44*, 11402–11411.
(65) Menil, F. *J. Phys. Chem. Solids* **1985**, *46*, 763–789.
(66) Parish, R. *NMR, NQR, EPR, and Mössbauer Spectroscopy in Inorganic Chemistry*; Ellis Horwood: New York, p 133 1990.

Table 2. Parameters Obtained by Fitting the Room-Temperature Mössbauer Spectra of the BSFA Samples[a]

	BSF		BSFA0.01		BSFA0.05		BSFA0.1		BSFA0.2			
	Fe^{4+}	Fe^{3+}	Fe^{4+}	Fe^{3+}	Fe^{4+}	Fe^{3+}	Fe^{4+}	Fe^{3+}	Fe^{4+}	Fe^{4+}	Fe^{3+}	Fe^{3+}
IS (mm/s)	−0.172(6)	0.182(5)	−0.173(1)	0.183(2)	−0.174(7)	0.183(9)	−0.173(7)	0.181(6)	−0.173(5)	−0.143(8)	0.102(9)	0.282(2)
QS (mm/s)	0.484(3)	0.702(8)	0.543(5)	0.724(6)	0.511(4)	0.721(8)	0.494(2)	0.734(4)	0.471(7)	0.832(4)	0.724(3)	0.802(6)
I(%)	36.4(7)	63.6(8)	35.5(3)	64.5(6)	34.0(3)	66.0(5)	31.9(2)	68.1(4)	21.4(3)	23.1(7)	11.9(5)	43.6(2)

[a] IS is the isomer shift relative to Fe in Rh at 293 K. QS is the quadrupole splitting.

subspectra. On the basis of the information that the sample contains more than one phase, we have fitted its spectrum with four components. The analysis of the spectrum revealed the presence of two nonequivalent sites for both Fe^{3+} and Fe^{4+} cations. The hyperfine parameters obtained by fitting the spectra of the $(Ba_{0.5}Sr_{0.5})(Fe_{1-x}Al_x)O_{3-\delta}$ samples are listed in Table 2. As shown in Table 2 and Figure 4b, the intensity of the doublet corresponding to Fe^{3+} cations increases monotonically with increasing Al-substitution. Thus, Al-addition increases the proportion of trivalent iron in $(Ba_{0.5}Sr_{0.5})(Fe_{1-x}Al_x)O_{3-\delta}$, as has already been observed for Ga-doped $SrFeO_{3-\delta}$ based phases[67] and similar compositions with tetravalent B-site dopants.[43,68] The quadrupole splitting value characteristic of Fe^{3+} cations slightly increases with Al content, indicating greater disorder around Fe^{3+}. Similarly as in the work of Waerenborgh et al.,[40] it can be assumed that the Al-doping leads to a localization of electron states around oxygen by introducing greater ionic character to the Fe−O−Fe network. In summary, Mössbauer results show Fe^{4+} and Fe^{3+} cations both in the high-spin state and greater disorder around Fe^{3+}, which with respect to EELS can also be interpreted as less covalent mixing of the iron d- and oxygen p-orbitals, resulting in an expanded perovskite lattice.

Table 1 labels the weighted values for the crystallographic B-position in the perovskite lattice including aluminum. It is evident that the ratio of Fe^{3+} is almost constant. This leads to the conclusion that aluminum replaces predominantly Fe^{4+} in the lattice. There are two competing effects during the aluminum incorporation. First, Fe^{4+} and Al^{3+} have similar ionic radii, but the oxygen deficit has to be increased due to the lowering of charge. Second, Fe^{3+} and Al^{3+} have the same oxidation state, but different ionic radii. The second effect seems to be the weaker driving force, compared to the effect of the similar radius, hence most of the Al^{3+} replaces Fe^{4+} in the lattice. This causes a higher oxygen vacancy concentration, which is increased even more with rising temperature because of oxygen removal. The material might not be stable at higher temperatures and even collapse into brownmillerite phase with $ABO_{2.5}$ stoichiometry.[69] To examine the high temperature stability of the $(Ba_{0.5}Sr_{0.5})(Fe_{1-x}Al_x)O_{3-\delta}$ perovskites, in situ XRD and TG/DTA measurements were conducted. The in situ XRD measurements of BSFA0.1 are shown in Figure 5. The sample was heated from 35 to 1000 °C and cooled again in steps of 200 °C in ambient air. The cubic perovskite phase is stable over the whole temperature range. Because of the thermal expansion of the material, a shift of lattice parameters of 0.0063 nm is evident, and the CTE was determined to be 16×10^{-6} K^{-1}.

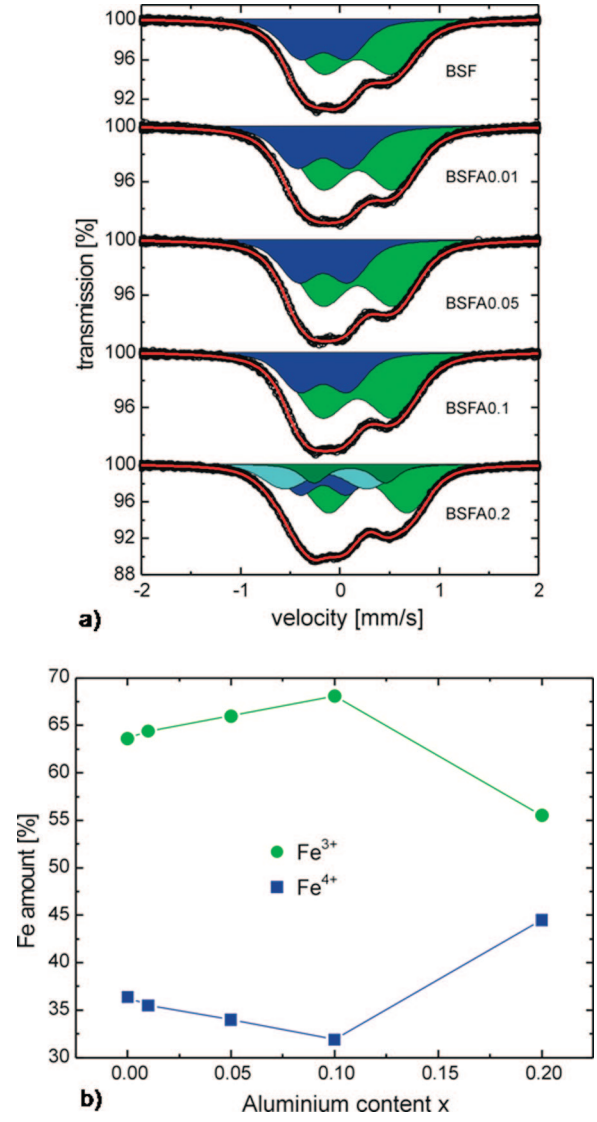

Figure 4. Mössbauer results for (a) room-temperature spectra of BSF, BSFA0.01, BSFA0.05, BSFA0.1, and BSFA0.2; (b) variation of the amount of Fe^{3+} and Fe^{4+} cations in BSFA samples with respect to total iron content (≠ total B-site occupancy) as a function of Al content.

TG/DTA measurements revealed that the perovskites are stable until 1350 °C. Above that temperature a decomposition slowly sets in, and the definitive melting points (T_{mp}) are between 1380 and 1400 °C (T_{mp}(BSF) = 1381 °C, T_{mp}(BSFA0.01) = 1392 °C, T_{mp} (BSFA0.05) = 1389 °C, T_{mp} (BSFA0.1) = 1399 °C, T_{mp}(BSFA0.2) = 1356 °C). BSFA0.01 exhibits the highest stability. Because of the knowledge of the decomposition and melting points, the sintering temperature for the perovskite membranes could

(67) Patrakeev, M. V.; Mitberg, E. B.; Lakhtin, A. A.; Leonidov, I. A.; Kozhevnikov, V. L.; Kharton, V. V.; Avdeev, M.; Marques, F. M. B. *J. Solid State Chem.* **2002**, *167*, 203–213.
(68) Adler, P.; Eriksson, S. *Z. Anorg. Allg. Chem.* **2000**, *626*, 118–124.
(69) McIntosh, S.; Vente, J. F.; Haije, W. G.; Blank, D. H. A.; Bouwmeester, H. J. M. *Solid State Ionics* **2006**, *177*, 833–842.

Table 3. Summary of Average Grain Size Areas (A_{gs}) and Oxygen Permeation Flux (J_{O_2}) with Oxygen Partial Pressure of the Permeate Side (p_{O_2}) of Sintered Membranes at 900 °C

membrane	A_{gs} [μm]	J_{O_2} (mL cm^{-2} min^{-1})	p_{O_2} [$\times$ 10^3 Pa]
BSF	166	0.61	1.3
BSFA0.01	75	0.76	1.5
BSFA0.05	146	0.83	1.7
BSFA0.1	10	0.98	2.0
BSFA0.2	0.41	0.55	1.2

be chosen as high as 1150 °C. XRD measurements of the surfaces and fracture surfaces of the membranes were similar to those in Figure 1. Previous to oxygen permeation measurements, membranes were carefully checked for density, i.e., crack or channel formation, and depletion or accumulation of any element by SEM. Additionally, the grain size distribution and the correlation between grain size and oxygen permeation were investigated.

Figure 6 illustrates the scanning electron micrographs of the membrane surfaces and the grain size distributions of all sintered membranes. The membranes do not show cracks or channels; only some small pores are visible at the surface, which are not connected throughout the membrane. This was evidenced by SEM of the fracture surfaces.

Grain size distribution was the same for surfaces and fracture surfaces for each kind of membrane. This was already demonstrated for $(Ba_{0.5}Sr_{0.5})(Fe_{0.8}Zn_{0.2})O_{3-\delta}$ and $(Ba_{0.5}Sr_{0.5})(Co_{0.8}Fe_{0.2})O_{3-\delta}$.[70] Table 3 summarizes the average grain size areas A_{gs} and shows that they are very different for the BSFA membranes and do not correlate with the aluminum doping. Membranes of BSF have the biggest A_{gs} with 166 μm. Grain sizes for the pure phases BSFA0.01 and BSFA0.05 increase and decrease again as soon as impurities are formed for BSFA0.1 and BSFA0.2. The formation of the other phases inhibits the grain growth.

Because mappings by EDXS of the surfaces and fracture surfaces showed a homogeneous distribution of all elements without any depletion or accumulation, they are not presented here. The quantification confirms the stoichiometries

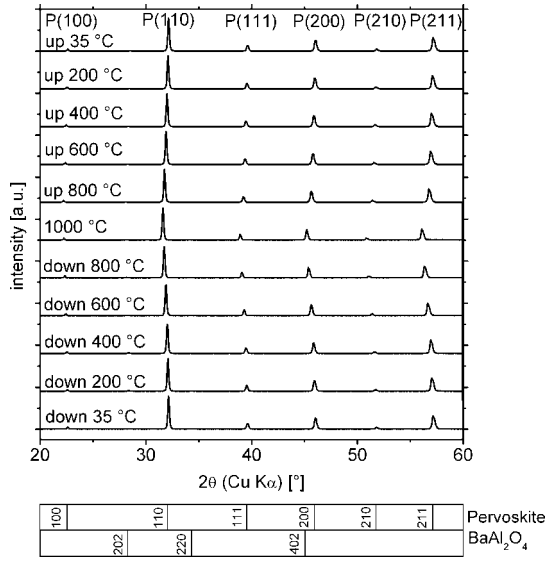

Figure 5. In situ X-ray diffraction data for BSFA0.1 (calcined at 950 °C for 10 h), heated from 35 to 1000 °C and cooled again in steps of 200 °C (heating rate 5 K/min) with an equilibrium time of 1/2 h in ambient air.

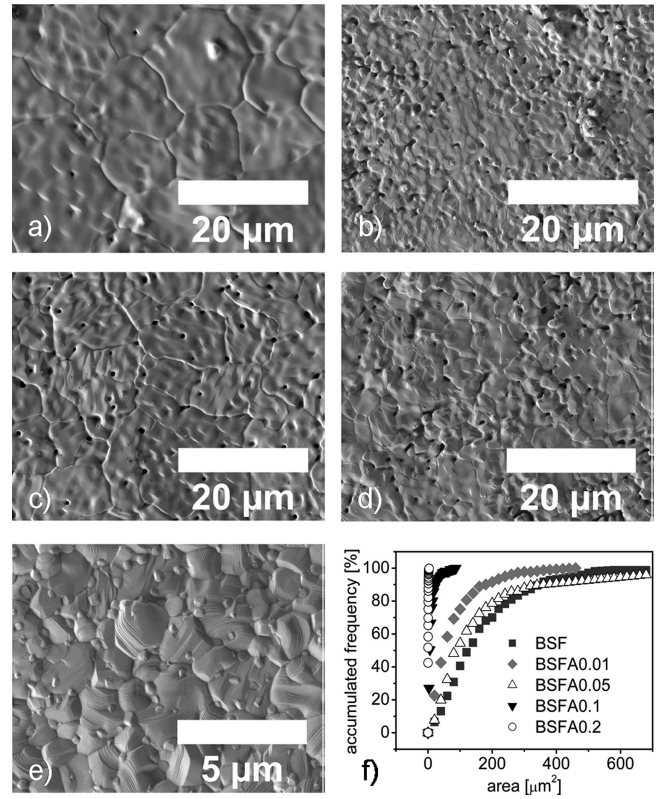

Figure 6. Scanning electron micrographs showing surfaces and grain size distributions at 1150 °C for 10 h of sintered membranes (a) BSF, (b) BSFA0.01, (c) BSFA0.05, (d) BSFA0.1, (e) BSFA0.2 (note different scale), and (f) grain size area distribution.

$(Ba_{0.5}Sr_{0.5})(Fe_{1-x}Al_x)O_{3-\delta}$ with $0 \leq x \leq 0.2$, respectively. Hence, BSFA0.1 and a BSFA0.2 membranes were prepared for TEM. We were interested in seeing if the impurities are located in the grain boundaries or as separate particles. Figure 7 shows a transmission electron micrograph of BSFA0.1 and the element distribution of oxygen, aluminum, barium, iron, and strontium. The impurity phases were found to be located as separated grains in the perovskite grains. The higher aluminum fraction of the $BaAl_2O_4$ can be seen in Figure 7c. Micrographs e and f in Figure 7 show a weak signal of iron and strontium for the $BaAl_2O_4$ phase, which was quantified as a small solubility of 3% strontium of the barium site and 8% iron of the aluminum site. The latter was also reported by Yaremchemko et al. for a iron solubility in $SrAl_2O_4$ below 5% of the aluminum sites and by Kharton et al. below 7%.[42,32] The perovskite in BSFA0.1 and BSFA0.2 was quantified as $(Ba_{0.48}Sr_{0.52})(Fe_{0.91}Al_{0.09})O_{3-\delta}$ with slight deviations very close to impurity grains.

For an impression of the application of BSFA materials, the oxygen permeation behavior was investigated. The oxygen permeation results are displayed in Figure 8. Figure 8a shows the temperature dependence for membranes with different aluminum fractions in comparison to the data of a BSF membrane measured by Chen et al.[71] The oxygen permeation increases with rising Al content from 0 to 0.1 to a maximum of 1.19 mL cm^{-2} min^{-1} at 950 °C and decreases again for BSFA0.2 to values comparable to those for BSF. The activation energies were calculated from the oxygen permeation and were found to decrease from 86 kJ mol^{-1}

Table 4. Oxygen Permeation Flux Across Different Membranes with Iron and Aluminum at the B-Site Compared to Other Perovskite Materials Containing Barium on the A-Site of the Lattice[a]

perovskite membranes	thickness (mm)	oxygen permeation flux (mL cm $^{-2}$ min $^{-1}$)			
		800 °C	850 °C	900 °C	950 °C
$(Ba_{0.5}Sr_{0.5})(Fe_{1-x}Al_x)O_{3-\delta}$ ($x = 0.1$)	1.1	0.63	0.82	0.98	1.19
$Sr(Fe_{1-x}Al_x)O_{3-\delta}$ ($x = 0.3$) [36]	1.0	0*	0.05	0.13	0.20
$(La_{0.3}Sr_{0.7})(Fe_{1-x}Al_x)O_{3-\delta}$ ($x = 0.2$) [35]	1.0	0.05	0.08	0.13	0.21
$(Ba_{0.5}Sr_{0.5})(Fe_{0.8}Zn_{0.2})O_{3-\delta}$ [50]	1.15	0.49	0.65	0.80	0.96
$(Ba_{0.5}Sr_{0.5})(Co_{0.8}Fe_{0.2})O_{3-\delta}$ [19]	1.5	0.92**	1.18**	1.39	1.57
$Ba(Co_xFe_yZr_z)O_{3-\delta}$ ($x + y + z = 1$) [72]	1.0	0.5	0.6	0.7	0.8*

[a] The oxygen partial pressure at the permeate side for BSFA was in the range of $0.7-2.4 \times 10^3$ Pa. Values marked with * are extrapolated with the assumption of a linear gradient of the oxygen permeation flux depending on the temperature. Those marked with ** are not stable for a long time (≥300 h).[19−21]

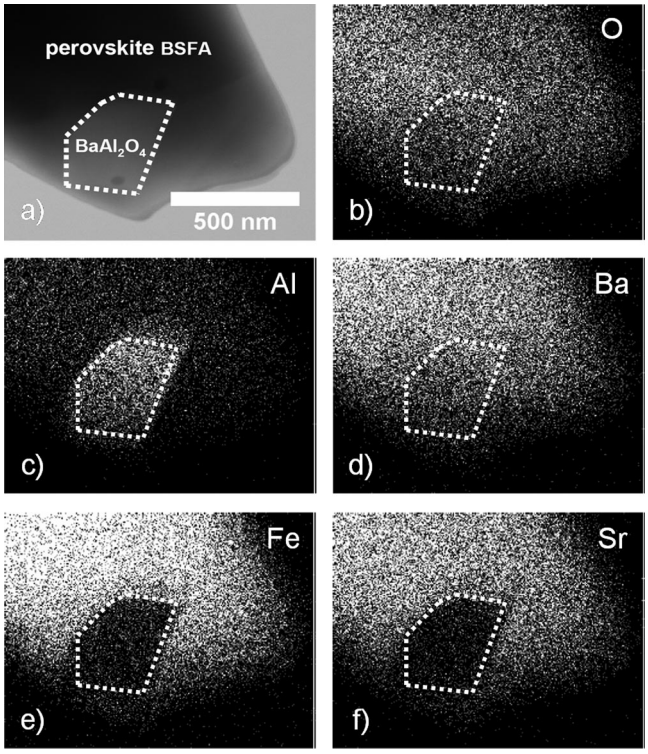

Figure 7. Scanning transmission electron micrograph of BSFA0.1 (a) and element distribution of (b) oxygen, (c) aluminum, (d) barium, (e) iron, and (f) strontium.

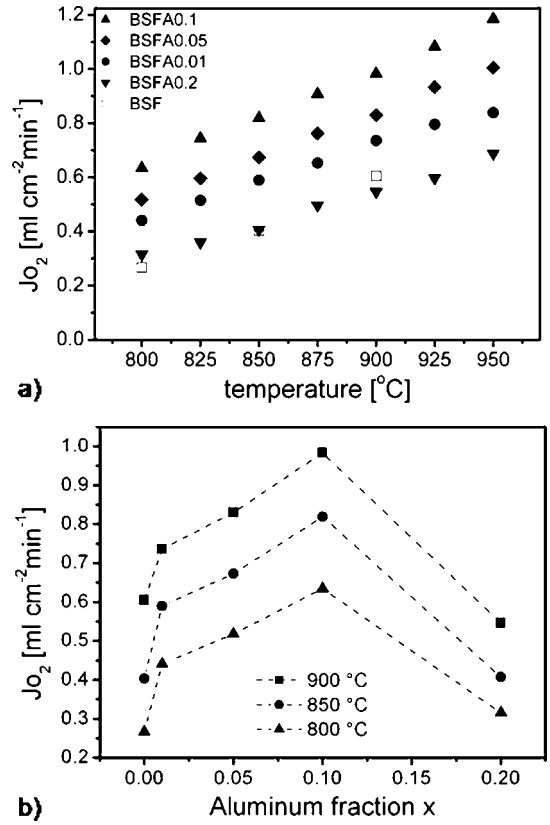

Figure 8. Oxygen permeation flux: (a) temperature dependence for BSF,[71] BSFA0.01, BSFA0.05, BSFA0.1, and BSFA0.2, membrane thickness = 1.1 mm; (b) for membranes with various aluminum fractions at different temperatures. The lines are guides for the eye and indicate a maximum at an Al fraction of 0.1. The oxygen partial pressure at the permeate side was in the range of $0.7-2.4 \times 10^3$ Pa.

for BSF to 44 kJ mol^{-1} for BSFA0.1 and increase again for BSFA0.2 (57 kJ mol^{-1}). The change in oxygen permeation for membranes with varying aluminum fractions at different temperatures is presented in Figure 8b. The maximum for BSFA0.1 demonstrates that the very small impurity of 3.3% does not disturb the oxygen transport through the membranes, but a higher impurity content of 14% (BSFA0.2) leads to a decrease in oxygen permeation.

We also found that oxygen permeation depends primarily on the materials composition and not on the grain size (Table 3). In spite of the reduction in grain size from BSF to BSFA0.01, the oxygen permeation rises; however, with increasing grain size from BSFA0.01 to BSFA0.05, a further rise in permeation is observed. Because of the impurity in BSFA0.1, the grain growth was inhibited, but the permeation increases even more. Further measurements for oxygen permeation dependence on grain size for each composition are required to draw final conclusions. The BSFA0.1 membranes show high oxygen permeation in comparison to the currently known perovskite membranes labeled in Table 4. Among the Fe- and Al-containing membranes, they have the highest oxygen permeation. Only $(Ba_{0.5}Sr_{0.5})(Co_{0.8}Fe_{0.2})O_{3-\delta}$, the current state-of-the-art material above 900 °C, reaches higher values.[1] However, in the intermediate temperature range the novel aluminum doped perovskite BSFA0.1 is expected to show a better performance in application than the cobalt containing BSCF because of an improved long-time stability preserved by a less flexible redox behavior and a stable high-spin configuration of iron.

(70) Arnold, M.; Martynczuk, J.; Efimov, K.; Wang, H.; Feldhoff, A. *J. Membr. Sci.* **2007**, *316*, 137–144.
(71) Chen, Z.; Ran, R.; Zhou, W.; Shao, Z.; Liu, S. *Electrochim. Acta* **2007**, *52*, 7343–7351.
(72) Wang, H.; Schiestel, T.; Tablet, C.; Schroeder, M.; Caro, J. *Solid State Ionics* **2006**, *177*, 2255–2259.

Conclusions

The systematic aluminum doping of $(Ba_{0.5}Sr_{0.5})(Fe_{1-x}Al_x)O_{3-\delta}$ was conducted in the range of $0 < x \leq 0.2$ with regard to the calculation of the tolerance factors. With XRD, the perovskite phase in all synthesized oxides was found to be cubic perovskite, and the highest aluminum fraction for a formation of pure cubic perovskite without any impurities was in the range of $x = 0.09-0.1$. In the BSFA0.1 powder, a minor impurity (3.3%) of $BaAl_2O_4$ was determined by Rietveld refinements, and for BSFA0.2, two impurities were found and identified as $BaAl_2O_4$ and $Ba_3Al_2O_6$. The impurity phases are located as separated grains in the perovskite grains (TEM). Because of the smaller ionic radius of aluminum, the lattice parameters were expected to decrease. However, the reverse was found by XRD. EELS together with Mössbauer spectroscopy revealed that with the increasing replacement of iron with aluminum at the B-position of the perovskite ($x \leq 0.1$), a higher fraction of Fe^{3+} instead of Fe^{4+} is observed and because of the decreased covalent mixing of the iron 3d and oxygen 2p orbitals the lattice expands. Fe^{4+} is predominantly substituted by Al^{3+} because of their similar ionic radii, but with this substitution the oxygen deficit has to be increased. This results in a higher oxygen vacancy concentration, which might cause instability of the material at higher temperatures. However, in situ XRD and TG/DTA measurements reveal high temperature stability up to 1350 °C. The oxygen permeation increases with rising Al content from 0 to 0.1 to a maximum of 1.19 mL cm^{-2} min^{-1} at 950 °C and decreases again for BSFA0.2 to values comparable to BSF. The maximum for BSFA0.1 demonstrates that the very small impurity does not disturb the oxygen transport through the membranes. We also found that the oxygen permeation is primarily dependent on the materials composition, because the grain size is not directly correlated with the oxygen permeation. The BSFA0.1 membranes show very high oxygen permeation, in comparison to the currently known perovskite membranes. Additionally, among the iron and aluminum containing membranes they have the highest oxygen permeation. Because of an improved long-time stability preserved by a less-flexible redox behavior and a stable high-spin configuration of iron, a good performance in the intermediate temperature range, where cobalt containing perovskites have serious stability problems, is expected in application.

Acknowledgment. The authors greatly acknowledge financial support by DFG Grant FE 928/1-2. Fruitful discussions with Prof. Jürgen Caro are appreciated. V.Š. thanks the APVV (Project 0728-07) and VEGA (2/0065/08) for their support of his work.

CM803217T